Preliminary Evaluation of Angular Reflectance Downscaling Using FSDAF Spatiotemporal Fusion Model and MODIS BRDF Data

Man Liang, Xingfa Gu, Yan Liu, Tianhai Cheng, Hongtao Cao, Hu Zhang, Qian Zhang, Yaozong Ding, Min Gao, Xiangqin Wei, and Yulin Zhan

***Abstract*—As the resolution of remote sensing quantitative inversion for albedo, clumping index, canopy height, and other biophysical parameter data is gradually refined, there is an increasing demand for higher spatial resolution bidirectional reflectance distribution function (BRDF) and angular reflectance data. In this article, we applied and evaluated flexible spatiotemporal data fusion to downscale angular reflectance using low-resolution BRDF data (MCD43A1) and high-resolution Sentinel-2 data as inputs. We selected Sentinel-2 orbital overlap regions with various anisotropic flat index (AFX) types and overpassing times as the study area as to obtain angular reflectance data under different anisotropic and solar-viewing geometry conditions. We found that the fusion method can downscale the angular reflectance with high accuracy (root mean square error < 0.04, bias < 0.02). The downscaling accuracy was higher in the cross-principle plane than in the principle plane, whereas there was no significant variation in accuracy under different AFX conditions. Owing to the lack of angular surface reflectance at larger viewing angles, validation was performed only within a view zenith angle of 10.3°. Further validation using satellites with larger viewing angles, such as Gaofen-6 or unmanned aerial vehicles, can be used to evaluate the accuracy of this method. This article presents a strategy for downscaling angular information, preliminary validation results, and satellite-based evidence of scale effects between the 500–10 m scales of the BRDF.**

***Index Terms*—Angular reflectance downscaling, anisotropic flat index (AFX), bidirectional reflectance distribution function (BRDF), spatiotemporal fusion.**

Manuscript received 1 September 2023; revised 16 January 2024; accepted 9 February 2024. Date of publication 14 February 2024; date of current version 23 February 2024. This work was supported in part by the National Key R&D Program of China under Grant 2021YFE0117300, in part by the National Natural Science Foundation of China under Grant 41901367, and in part by the Major Project of High Resolution Earth Observation System under Grant "30-Y60B01-9003-22/23." *(Corresponding author: Yan Liu.)*

Man Liang, Yan Liu, Tianhai Cheng, Hongtao Cao, Qian Zhang, Yaozong Ding, Min Gao, Xiangqin Wei, and Yulin Zhan are with Aerospace Information Research Institute, Chinese Academy of Sciences, Beijing 100049, China, and also with the University of Chinese Academy of Sciences, Beijing 101408, China (e-mail: liangman21@mails.ucas.ac.cn; liuyan@aircas.ac.cn; chength@aircas.ac.cn; caohongtao0714@163.com; zhangqian221@mails.ucas.ac.cn; dingyaozong22@mails.ucas.ac.cn; 13834587699@183.com; weixq@aircas.ac.cn; zhanyl@aircas.ac.cn).

Xingfa Gu is with Aerospace Information Research Institute, Chinese Academy of Sciences, Beijing 100049, China, and also with the School of Remote Sensing and Information Engineering, North China Institute of Aerospace Engineering, Langfang 065000, China (e-mail: guxf@aircas.ac.cn).

Hu Zhang is with the School of Geographic and Environmental Sciences, Tianjin Normal University, Tianjin 300387, China (e-mail: huzhang@tjnu.edu.cn).

Digital Object Identifier 10.1109/JSTARS.2024.3365826

I. Introduction

THE bidirectional reflectance distribution function (BRDF) describes the relationship between radiation received from one direction and radiation emitted from another outgoing direction within a hemisphere [1]. This function reflects the anisotropy characteristics of the surface. In the field of quantitative remote sensing, the BRDF serves as a pivotal parameter in the inversion of surface albedo, clumping index (CI), biomass, canopy height, and classification [2], [3], [4], [5], [6], [7], [8]. Moreover, the BRDF is key in addressing surface reflectance variability caused by observation-illumination geometry and surface heterogeneity [9].

To retrieve the BRDF, it is vital to obtain multiangle observations using appropriate angular sampling schemes. Sparse angular sampling from satellites introduces uncertainty into the inversion process [10]; however, the ability of satellites to capture angular observations at both low and high resolutions differs considerably.

At lower resolutions (greater than 250 m, the finest MODIS resolution), there are three primary methods for obtaining multiangle satellite data: 1) acquiring multiangle observations simultaneously in the orbital direction by adjusting the inclination of the sensor, such as CHRIS [11], [12] on the PROBA satellite, or carrying multiple cameras with different angles, like MISR on the Terra satellite [13]; 2) obtaining data from the overlapping portion of the multiviews along their orbits and crossing neighboring orbits through a charged coupled device matrix array detector, such as POLDER [14] on PARASOL; and 3) obtaining multiangle observations by crossing neighboring orbits using scanning sensors with a wide field of view (FOV), such as in NOAA–AVHRR [15], Terra/Aqua-MODIS [16], VIIRS [17], SPOT-VEGETATION [18], and FY3-VIRR/MERSI [19]. These sensors all have scanning zenith angles greater than 50° and a revisit period of one day, enabling the collection of sequential multiangle observations over a period of hours or days. The retrieval of BRDF from the angular sampling provided by these multiangle data can be achieved through the inversion of a kernel-driven BRDF model.

However, existing high-resolution (10–30 m) satellites are unable to provide near-synchronized multiangle observations with a relatively small FOV and extended revisit period. Even when considering the orbital overlap obtained over several days,

there is still a lack of angular sampling, either across or along the track, owing to the constraints of its small FOV. This limitation is evident in satellite systems, such as the Sentinel series (Europe) [20], the Landsat series (USA) [21], the Huanjing (China) [22], and the Gaofen (China) [23]; in these systems, scanning zenith angles are smaller than 40°, and revisit periods are longer than two days. As a result, relying only on high-resolution satellites cannot yield reliable accuracy in the retrieval of higher resolution BRDF.

In addition to the need for inversion of high-resolution BRDFs, there is also an increasing demand for angular reflectance in a number of other fields. Taking the Nadir BRDF adjusted reflectance (NBAR) at Nadir downward looking angles as an example, first, it is beneficial for data comparison and fusion between different sensors as it corrects the observation angle differences; second, the results are more stable when using NBAR as an input to the backend model. The inversion of some parameters depends on the reflectance at specific angles, and the best performance of some spectral indices is also obtained at specific combinations of angles, such as the estimation of CI using the normalized difference between hotspot and darkspot method [2], and the inversion of particle size of granite using multiangle hyperspectral data [24]. In the case of the PROSPECT 5B + 4SAIL radiative transfer modeling for geobiophysical plant variables, the Nadir data were superior in LAI retrieval accuracy while the off-Nadir data were more accurate in leaf chlorophyll content inversion [25].

Given that current high-resolution satellites lack the capability to directly obtain multiangle observations, downscaling methods are required to fuse existing products and harness the advantages of both high and low spatial resolutions.

Existing strategies that utilize coarse-resolution satellite data (e.g., MODIS BRDF) as a bridge for cross-scale applications are mainly categorized into lookup table (LUT) methods, a priori prototyping methods, fixed-parameter methods, and unmixing methods.

The LUT method, under the assumption that BRDF is related to land cover and independent of scale, associates factors, such as surface land cover, season, degree of disturbance, DEM, etc., with BRDF parameters to form an LUT, which is applied to high-resolution imagery for albedo inversion; Shuai et al. [26] first used MODIS BRDF parameters for Landsat albedo inversion and validated it using SURFRAD and MCD43A3 data, which were later developed into the statistical BRDF LUT method [27], thus making albedo inversion independent of MODIS products and enabling albedo production on Landsat data from the pre-MODIS period. Further, Gao et al. [28] optimized the LUT method for normalized difference vegetation index (NDVI) over land cover thresholds; and He et al. [29] built an LUT considering the BRDF effect directly from top-of-atmosphere reflectance and albedo, thus reducing the error due to atmospheric correction.

Assuming the BRDF parameters have no obvious connection with land cover or NDVI, the priori prototype method classifies the BRDF shapes based on anisotropic flat index (AFX) [30], and the prototypes derived from the classification can be independent of scales and represent most of the anisotropic features. Zhang et al. [31] compared and validated the albedo inversion effects of the BRDF parameters by weighted average with those counted according to land cover and NDVI segmentation. They found that the dominant shape of the region can represent most of the anisotropy of the image and control the accuracy within a certain range, except the case of the parameter that has multiple aggregation centers.

The fixed-parameter method statistically averages the coarse-resolution BRDF parameter corresponding to a large number of high-resolution satellite orbit overlap regions, which is used as parameters for NBAR correction. Roy et al. [32] applied this fixed parameter to Landsat 5TM, Landsat7 ETM+, and Sentinel-2 for NBAR generation [33], and Claverie et al. [34] applied the method to the Landsat and Sentinel data assimilation to generate the HLS dataset. The method has the advantages of being computationally efficient, insensitive to land cover, and resistant to disturbance, but it is not recommended for SZA $> 50°$, sensors with wide viewing angle variations, or albedo inversion.

The unmixing method normalizes the semiempirical model into two shape parameters, R and V, before downscaling the MODIS BRDF parameters at 1-km climate mode resolution to the target resolution by hybrid pixel unmixing based on unsupervised classification. This method has been used on Landsat albedo inversion as well as on corrective validation of HLS fusion products [35], [36]. Validated for SURFRAD and OzFlux sites, it was found that the angular reflectance in the principle plane (PP) is more strongly associated with the VZA in the region near the Brazilian Amazon Forest; while the current HLS BRDF correction (fixed parameter method), although reducing this angular dependence, still shows undercorrection, especially in the near-infrared (NIR) bands.

These strategies aimed at albedo products or NBAR generation, and they may not be concerned with the accuracy of reflectance in a specific direction. In addition, their cross-scale adjustment algorithms take a relatively simple ratio adjustment method (C-factor method), which may produce a patchy effect when the resolution of BRDF data is much lower than that of the target high-resolution satellites. In order to further investigate the means of downscaling satellite angular reflectance data in other directions, this article introduces spatiotemporal fusion algorithms into the field to replace the general C-factor method.

Spatiotemporal fusion demonstrates qualities of robustness and simplicity, rendering it suitable for addressing discrepancies between different scales. Spatiotemporal fusion methods are primarily categorized into five types based on their assumptions and strategies [37]: weight-based [38], [39], unmixing [40], [41], Bayesian assumptions [42], learning [43], and hybrid methods [44], [45]. Hybrid methods, such as the flexible spatiotemporal data fusion (FSDAF), combine the advantages of several strategies [44]. In the past decade, these methods have been applied in various research areas, including crop detection, surface classification, and change detection [46], [47], [48], [49].

The common task of spatiotemporal fusion typically involves the downscaling of data at different points in time. Although it is rarely applied to multiangle data at present, we have applied it for different angles of downscaling in this article. An angular

TABLE I
EXPERIMENTAL AREA INFORMATION

ANGLE GROUP	AFX GROUP	AFX VALUE	A1-TIME	A2-TIME	Landcover	NDVI	LON	LAT
RED BAND								
PP	1	0.667	23-02-14	23-02-16	Woody Savannas	0.788	80.46°E	6.14°N
	2	0.719	22-06-10	22-06-12	Woody Savannas	0.721	81.30°W	35.02°N
	3	0.833	22-06-11	22-06-13	Grassland	0.622	97.95°W	38.23°N
	4	0.965	22-06-11	22-06-13	Cropland	0.380	97.83°W	38.29°N
	5	1.040	22-07-01	22-07-03	Barren	0.077	48.37°E	20.52°N
	6	1.266	22-07-11	22-07-14	Deciduous Broadleaf Forests	0.856	50.65°E	36.85°N
MID	1	0.639	22-11-19	22-11-21	Deciduous Broadleaf Forest	0.414	90.81°W	37.44°N
	2	0.783	22-07-05	22-07-07	Grasslands	0.089	36.82°E	2.38°N
	3	0.924	22-07-09	22-07-10	Woody Savannas	0.067	69.82°E	61.05°N
	4	0.880	22-06-11	22-06-13	Barren	0.756	110.72°W	38.53°N
	5	1.087	22-07-02	22-07-04	Barren	0.042	86.13°E	39.91°N
	6	1.619	22-07-09	22-07-11	Croplands	0.863	82.41°E	55.31°N
CPP	1	0.579	22-07-16	22-07-18	Savannas	0.495	62.63°W	24.91°S
	2	0.706	22-11-17	22-11-19	Woody Savannas	0.561	81.30°W	35.02°N
	3	0.810	22-01-22	22-01-24	Grassland	0.325	97.95°W	38.23°N
	4	0.936	22-06-01	22-06-02	Mixed Forests	0.588	53.54°E	66.62°N
	5	1.059	22-06-01	22-06-02	Permanent Wetlands	0.717	62.32°E	63.41°N
	6	1.363	22-06-11	22-06-12	Woody Savannas	0.746	25.33°E	65.34°N
NIR BAND								
PP	1	0.740	22-07-01	22-07-03	Open Shrublands	0.095	113.27°W	28.05°N
	2	0.836	23-02-14	23-02-16	Woody Savannas	0.788	80.46°E	6.14°N
	3	0.903	22-06-10	22-06-12	Woody Savannas	0.721	81.30°W	35.02°N
	4	1.011	22-07-01	22-07-03	Barren	0.077	48.37°E	20.52°N
	5	1.108	22-06-11	22-06-13	Grassland	0.622	97.95°W	38.23°N
	6	1.150	22-06-11	22-06-13	Cropland	0.380	97.83°W	38.29°N
MID	1	0.653	22-11-19	22-11-21	Deciduous Broadleaf Forest	0.414	90.81°E	37.44°N
	2	0.826	22-07-05	22-07-07	Grasslands	0.089	36.82°E	2.38°N
	3	0.951	22-06-11	22-06-13	Barren	0.067	110.72°W	38.53°N
	4	1.038	22-07-09	22-07-10	Woody Savannas	0.756	69.82°E	61.05°N
	5	1.071	22-07-02	22-07-04	Barren	0.042	86.13°E	39.91°N
	6	1.201	22-07-09	22-07-11	Croplands	0.863	82.41°E	55.31°N
CPP	1	0.778	22-07-12	22-07-15	Barren	0.081	69.59°W	21.74°S
	2	0.869	22-06-01	22-06-02	Mixed Forests	0.588	53.54°E	66.62°N
	3	0.904	22-01-22	22-01-24	Grassland	0.325	97.95°W	38.23°N
	4	0.995	22-06-11	22-06-12	Woody Savannas	0.746	25.33°E	65.34°N
	5	1.109	22-07-06	22-07-09	Open Shrublands	0.205	123.28°E	27.34°S
	6	1.204	22-07-02	22-07-04	Closed Shrublands	0.683	118.89°E	33.60°S

reflectance algorithm utilizing a spatiotemporal fusion algorithm and coarse-resolution BRDF information for the vegetation and ground surface domains is presented in this article. To the best of our knowledge, this is also the first attempt to combine BRDF with spatiotemporal fusion model.

The main contributions of this article are as follows.

1) The provision of a novel strategy for generating high-resolution angular reflectance from low-resolution BRDF data using the FSDAF fusion method.
2) The evaluation of accuracy across a wide range of surface BRDF variations, using solar-viewing angle and AFX as the main variables.
3) The demonstration of relevant evidence regarding the scale effects of the BRDF and topographic effects at two resolutions (500 and 10 m).

The rest of this article is organized as follows. Section II describes the geographic location of the study area and the data used for processing and validation. Section III outlines the fusion process and evaluation design, and Section IV displays the results and precision metrics. Section V gives discussion about the findings. Finally, Section VI concludes this article.

II. STUDY AREA AND DATA SOURCES

A. Study Area

The orbital overlapping regions of Sentinel-2, covering several sun-view geometrics and AFX types, were selected as the experimental areas. Fig. 1 shows the geographical distribution of the experimental area. Table I presents detailed information, including sensing dates, International Geosphere Biosphere Programme (IGBP) classification, NDVI, AFX, and specific locations within the region of overlapping orbits of the Sentinel satellites. The angular relationship of solar-viewing configurations can be divided into three categories: PP, cross-principle plane (CPP), and transition type (MID). AFX classifications are divided into six archetypes. "A1-time" refers to the

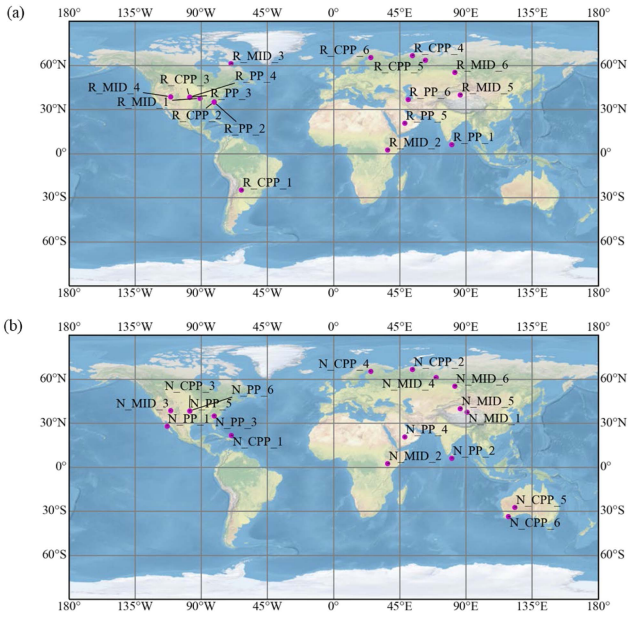

Fig. 1. Locations of experimental areas. Each region is denoted as "band_angle-group_afx-group." Here, R represents the red band, and N represents the near-infrared band. Due to the scale of map, some collision occurs in specific areas. In (a), R_PP_3 and R_CPP_3 represent the same region but in different seasons. R_PP_4 is situated in proximity. In (b), N_PP_5 and N_CPP_3 correspond to the same region but in different seasons. The region N_PP_6 is located nearby. The background raster map is sourced from Natural Earth Data (http://www.naturalearthdata.com), and the map was made using the Cartopy package [50].

sensing date of Sentinel-2 at angle-1 (A1), whereas "A2-time" refers to that of angle-2 (A2). This article focuses on the red and near- infrared bands. Since the AFX types corresponding to the two bands in the same region do not always coincide, the experimental areas targeting different bands were divided separately. In addition, since images from some of the experimental areas under different dates were also added for validation, there is some degree of overlap of labeled points in Fig. 1.

B. MODIS Products

The 500-m resolution MCD43A1 was used as the primary input for coarse-resolution surface BRDF information. By providing three weighting parameters corresponding to isotropy, volumetric scattering, and the geometric kernel, MCD43A1 can compute the surface reflectance under arbitrary illumination and observation angles using the RossThick-LiSparseR (RTLSR) BRDF model. To ensure a more stable BRDF data input, the quality assessment (QA) band of MCD43A1 was used to control its quality, and only pixels of the highest quality (QA = 0) were used in this method. Furthermore, coregistration with high-resolution data is required for coarse-resolution angular reflectance data.

To evaluate the performance of this method across different surface cover types, 500-m MCD12Q1 data were used. IGBPs with >50% of the pixels in the area became the dominant ground cover in the experimental area. MODIS data were obtained from the Google Earth Engine (GEE) platform: https://developers.google.com/earth-engine/datasets/catalog/MODIS_061_MCD43A1; https://developers.google.com/earth-engine/datasets/catalog/MODIS_061_MCD12Q1.

C. Sentinel-2 Surface Reflectance Product

The Sentinel-2 satellite constellation consists of two virtually identical polar-orbiting satellites, equipped with subtly distinct sensors. As part of the European Space Agency's (ESA's) program to detect changes, this satellite has the capability to capture imagery of the Earth's surface within the range of 56°S–84°N. This imaging is conducted with a revisit frequency of under five days, with observation zenith angles of up to 10.3°. Across 13 bands of varying resolutions, the satellite notably demonstrates its high-resolution capability through its 10-m resolution in the visible and NIR range. The RED and NIR bands of Sentinel-2 surface reflectance used in this article were obtained from the GEE platform: https://developers.google.com/earthengine/datasets/catalog/COPERNICUS_S2_SR.

Corresponding to each region, two views of Sentinel-2 data on different dates were selected as the source images, with one day serving as the input for downscaling, and the other as the validation of the target angle. These views correspond to closely timed observations, with a maximum interval of less than three days. Therefore, it can be assumed that the surface anisotropy did not change significantly during this period, and the sun illumination angles remained stable. The sole distinction lies in their origins from two directions of overlapping orbits, leading to changes in the satellite observation zenith and azimuth angles.

For the Sentinel image, surface reflectance following atmospheric correction can be obtained directly from the GEE platform. This involves atmosphere-correction, cloud-masking, and data range adjustment, after which the 10-m resolution image under WGS84 is exported. Before fusion occurs, as described in [32], it is necessary to ensure that the input image pixels are of the same dimensions (10 m) and that their length and width represent integer multiples of the scale ratio (the ratio of the two resolutions specified in this method is 480:10 = 48).

III. Methodology

The flowchart of the entire strategy is shown in Fig. 2.

The overall description of the method is as follows, which has three parts:

In the angular reflectance downscaling generation part, the angular information file of Sentinel-2 image for fusion (denoted as Angle-1) is used to compute a coarse-resolution angular reflectance through the RTLSR model with the MCD43A1 BRDF data of the same date. This reflectance is paired with the Sentinel-2 image at Angle-1 as a coarse-fine image pair at the same angle and becomes part of the input to the FSDAF model. The coarse-resolution angular reflectance was then calculated again by pairing the MCD43A1 BRDF data from the same day with the angular information file corresponding to the Sentinel-2 image used for the test (denoted as Angle-2). This reflectance, since it uses a different angle than Angle-1, will be used as another input to the FSDAF model.

The processing flow of the FSDAF model consists of unsupervised classification of the fine-resolution input image;

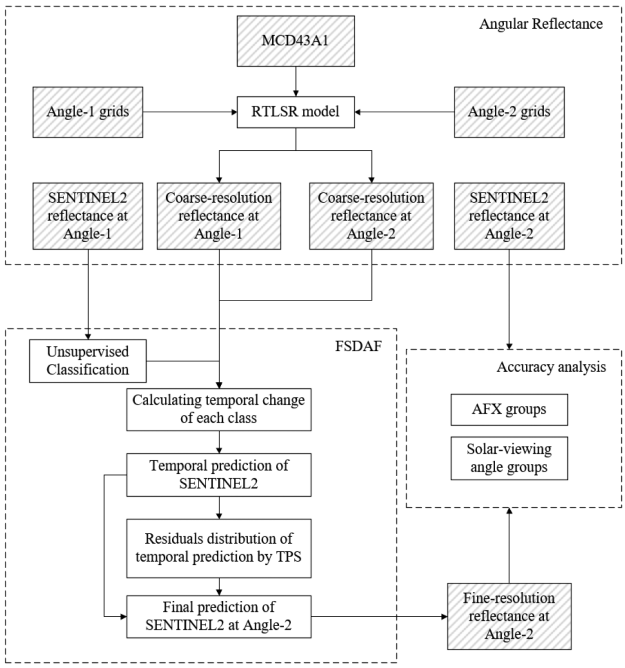

Fig. 2. Flowchart illustrating the angular reflectance downscaling strategy.

calculation of the change in pixels of the coarse-resolution image pair, where the anisotropic information from the different angles is regarded as a temporal surface change, which is further manifested in the difference in spectral intensities; and hybrid pixel unmixing of this change with the classification results of the fine-resolution, and the production of preliminary prediction results. The fine-resolution image at Angle-2 is finally generated by thin-plate spline interpolation (TPS) and residual optimization assignment.

For the sensitivity evaluation of the method, the solar-viewing angle relationship and the type of AFX were selected as the main categorical variables in the experimental area. Among them, the solar-viewing angle relationship is mainly determined by the relative azimuth angle (RAA), and the BRDF shape generally varies more drastically with the viewing angle when it is closer to the PP; the AFX is further normalized by the BRDF model, and its strength is related to the type of BRDF shape. The level of accuracy of this method can be assessed by comparing the real Sentinel-2 fine-resolution image at Angle-2 with the fine-resolution image generated by FSDAF. Visual assessment analyzes image quality and detail, and metrics used in quantitative assessment include root mean square error (RMSE), normalized RMSE (nRMSE), coefficient of determination (R2), and bias.

A. Angular Reflectance Downscaling Strategy

1) Angular Reflectance Data Generation: To simulate coarse-resolution surface reflectance at various angles, corresponding angular data and BRDF data were required as inputs. After acquiring the angle raster and MCD43A1, they were reprojected and resampled to normalize them to a spatial resolution of 480 m using the WGS84 geographic coordinate system. The BRDF was computed using the RTLSR model to calculate the surface reflectance at this observation-illumination geometry, detailed as follows:

$$R\left(\theta_s,\theta_v,\phi,\Lambda\right)=f_{\text{iso}}\left(\Lambda\right)+f_{\text{vol}}\left(\Lambda\right)K_{\text{vol}}\left(\theta_s,\theta_v,\phi\right)+f_{\text{geo}}\left(\Lambda\right)K_{\text{geo}}\left(\theta_s,\theta_v,\phi\right). \quad (1)$$

Here, $R(\theta_s,\theta_v,\phi,\Lambda)$ represents the directional reflectance of the surface, Λ denotes the specified wavelength, θ_s is the solar zenith angle, θ_v is the observation zenith angle, and ϕ is the RAA. These parameters describe the illumination-observation geometry. Additionally, K_{vol} and K_{geo} refer to the volumetric scattering kernel and the geometric-optical scattering kernel, respectively, and $f_{\text{iso}}(\Lambda)$, $f_{\text{vol}}(\Lambda)$, and $f_{\text{geo}}(\Lambda)$ are the coefficients of the three types of scattering.

In terms of the angle data of Sentinel-2, the GEE platform provides the average value instead of the corresponding angular raster. However, the actual Sentinel-2 image is captured through multiple subsensors, each having different orientations. To model the angular variations more accurately than an average value, it is necessary to obtain the original XML file for angle raster reconstruction and spatial interpolation. The XML file describes the solar zenith angle, solar azimuth, satellite zenith angle, and satellite azimuth information for each band at a 5-km resolution, and the resampling operation can be accomplished using the Sentinel Application Platform software provided by ESA or other processing methods.

2) FSDAF Fusion: Although various fusion models that require multiple pairs of inputs may produce improved results for angular reflectance, high-resolution data for input reference are limited due to the long revisit period. FSDAF combines unmixing, weight functions, and TPS interpolation into a unified framework, thus requiring only minimal inputs for most tasks while retaining high-quality details. In situations characterized by inadequate data availability, the FSDAF model is an appropriate choice, as it requires only one pair of different resolution images at T1 and a coarse-resolution image at T2 as the input; its output is a fine-resolution image at T2. In the context of angular reflectance downscaling, the task of this fusion algorithm is as follows. One pair of images with different resolutions at angle A1 and a coarse-resolution image at angle A2 are used as inputs, and the output is a fine-resolution image at angle A2.

The essence of the FSDAF revolves around finding the region of change in land cover between two images through single change detection and this alteration is then utilized as input to yield an optimal solution of the target estimation. Migrating it to multiangle tasks implies accepting the premise that a change in surface reflectance caused by the interaction of angle and BRDF is similar to land-cover changes that are strong enough to be detected. The algorithm comprises four main stages: unsupervised classification and detection of changing pixels, unmixing and prediction of temporal changes (multiangle in this task), TPS interpolation, and subsequent prediction, residual optimization, and the final prediction.

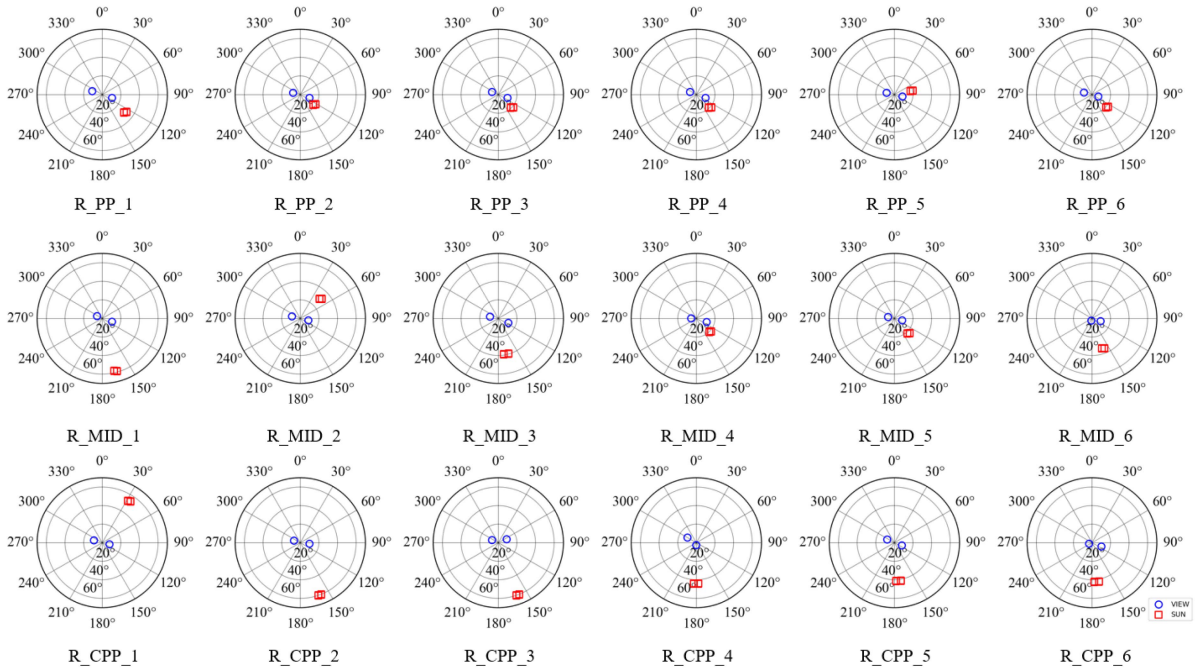

Fig. 3. Solar-viewing angle distribution in the study areas (RED band). The polar diameter of the polar chart represents the magnitude of the zenith angle, while the polar angle represents the azimuth (calculated clockwise from north). The blue circle indicates the satellite angle and the red square represents the sun angle.

B. Validation and Metrics

To evaluate the accuracy of angular reflectance prediction through fusion, the solar-viewing angular relationship and AFX were chosen as the criteria for the classification of the study area in the validation phase.

1) Satellite and Sun Angle Distribution: For solar-viewing angular relations, three types were classified: PP, CPP, and MID. The RAA [the difference between the viewing azimuth angle (VAA) and sun azimuth angle (SAA)] was calculated to determine these classifications. RAA values smaller than 30° or greater than 150° were designated as part of the PP group; those within the range of 60°–120° of the CPP plane were labeled as the CPP group, and the remining values were assigned to the MID group. When the satellite orbital inclination remains stable, this angular relationship is primarily determined by the SAA, specifically by a combination of the local latitude and day of year.

To visually represent the difference in observation angles within the overlapped orbital region for transit dates of Sentinel satellites, the observation and sun angle statistics corresponding to the sensing dates in each region are shown in Figs. 3 and 4.

2) AFX: The RTLSR model introduces three parameters for each band to characterize the BRDF of ground pixels. To compare the BRDF across different bands, the AFX was proposed as a measure of the shape of the BRDF [30]. AFX can be calculated using (1) by $f_{\text{iso}}(\Lambda)$ and performing a hemispherical integration, shown as follows:

$$\text{AFX} = 1 + \frac{f_{\text{vol}}(\Lambda)}{f_{\text{iso}}(\Lambda)} H_{\text{vol}} + \frac{f_{\text{geo}}(\Lambda)}{f_{\text{iso}}(\Lambda)} H_{\text{geo}}. \tag{2}$$

TABLE II
AFX RANGE INFORMATION

Group	AFX Range (RED)	AFX Range (NIR)
1	0.382—0.680	0.541—0.804
2	0.680—0.795	0.804—0.896
3	0.795—0.899	0.896—0.966
4	0.899—1.026	0.966—1.042
5	1.026—1.240	1.042—1.142
6	1.240—1.946	1.142—1.361

H_{vol} and H_{geo} are the hemispherical integral values of the volumetric scattering and geometric-optical scattering kernels, which are 0.189184 and −1.377622 for the RTLSR model, respectively.

After normalization, the factors affecting the size of the AFX were reduced to two: the coefficients of the volumetric (vol) and geometric (geo) kernels. The change in the six types of AFX symbolizes the change in the shape of the BRDF from a roof-like configuration to a bowl-like shape; in other words, the role of geometric-optical scattering gradually gives way to volumetric scattering. The adopted AFX classification criteria were obtained from global MODIS classification results [30]. The specific values are shown in Table II.

One phenomenon is worth mentioning in the study of AFX. The relation among the range of AFX classified by ISODATA, MODIS IGBP, and NDVI is not obvious, with arbitrary AFX archetypes corresponding to rich ranges of IGBP types, and single IGBPs being difficult to classify into fixed AFX archetypes. Overall, AFX is more strongly associated with intrinsic structural attributes, while IGBPs are influenced by phenology and

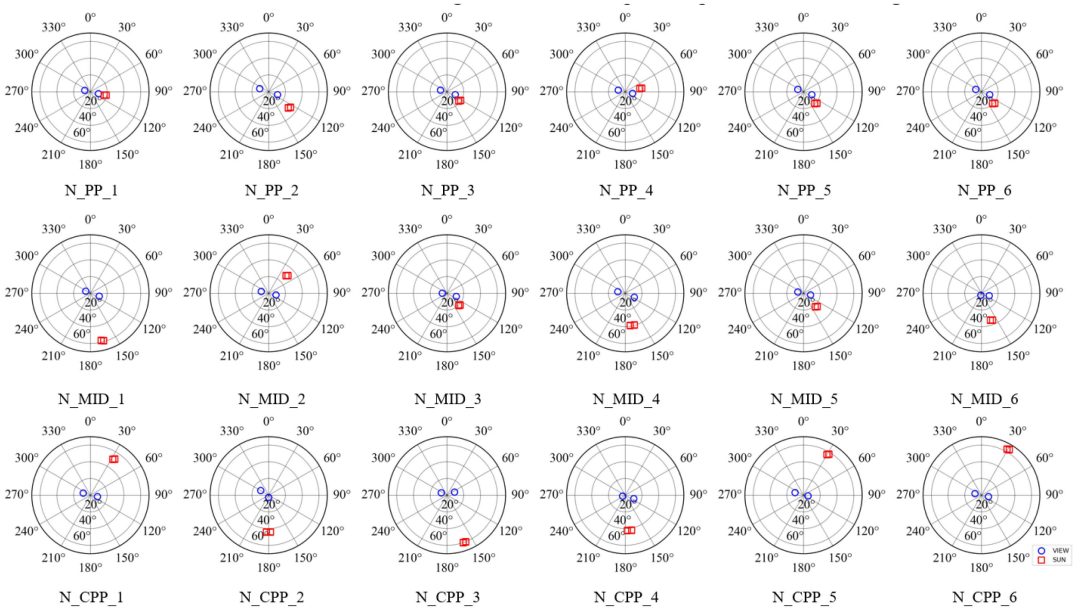

Fig. 4. Solar-viewing angle distribution in the study areas (NIR band). The polar diameter of the polar chart represents the magnitude of the zenith angle, while the polar angle represents the azimuth (calculated clockwise from north). The blue circle indicates the satellite angle and the red square represents the sun angle.

within-class variance. Therefore, the criterion chosen for the experimental area was mainly AFX, while IGBP and NDVI as reference values were also recorded in Table I.

3) Precision Indicators: This validation high-resolution Sentinel imagery and low-resolution MODIS-LIKE imagery at the A1 angle as input data, along with the MODIS-LIKE image at the A2 angle, to predict the Sentinel-2 image at the A2 angle. The evaluation used a real Sentinel image at the A2 angle as the ground truth. The precision indicators included bias, RMSE, nRMSE, and the R2. These values were calculated as follows:

$$\mathrm{RMSE} = \sqrt{\frac{1}{n-1}\sum_{i=1}^{n}(y_i - x_i)^2} \tag{3}$$

$$\mathrm{nRMSE} = \frac{\mathrm{RMSE}}{\bar{x}} \tag{4}$$

$$\mathrm{bias} = \mathrm{mean}\,(y - x) \tag{5}$$

$$R2 = \frac{\left[\sum_{i=1}^{n}(y_i - \bar{y})(x_i - \bar{x})\right]^2}{\sum_{i=1}^{n}(y_i - \bar{y})^2 \times (x_i - \bar{x})^2}. \tag{6}$$

IV. Results

A. Visual Assessment Result

The actual Sentinel images at A2 and the fusion results of the two bands are displayed in Figs. 5 and 6, respectively. In the visual evaluation, the fused images effectively retained most of the texture details while reflecting the reflectance variations due to angle changes.

However, the overall level of reflectivity differed somewhat from the true value, and a certain degree of overestimation and underestimation was observed based on the angular variance relationship (VAA and VZA). Since whether an observation angle is of the forward or backward type is not consistent with the Angle-1 and Angle-2 divisions (especially for the CPP case, for which the forward and backward directions are not obvious), the overestimation or underestimation of prediction results is also uncertain. In particular, for R_PP_6, R_MID_3, R_MID_6, R_CPP_5, N_CPP_5, and N_CPP_6, the difference between the two was more easily captured. In addition, a distinct band appeared at R_CPP_1. The performance of the NIR band was better than that of the RED band.

Regarding the fusion details, variations in performance were observed among each region. There were some geometric errors between the results of R_PP_1, R_PP_6, R_MID_4, N_MID_3, and their respective reference images. Changes in canopy, terrain, and surface were identified as the primary causes of the geometric errors between the two angles. In R_PP_1 and R_PP_6, the regions were characterized by savannas and forests, while R_MID_4 and N_MID_3 were located in areas with pronounced topographical differences. The results for R_PP_5 (N_PP_4, denoting the same location) and R_MID_5 (N_MID_5), encompassing dune areas with rapidly changing surfaces, showed textural details that were not consistent with the Sentinel-2 reference image. To the best of our ability, we attempted to mitigate the effect of surface changes when selecting the study area, but the constraints imposed by the solar-viewing angle and AFX criteria limited this choice.

B. Quantitative Assessment Result

The results of the scatterplot comparisons, summary plots for the indicators, and specific indicator values for each experimental area are summarized as follows. Fig. 7 shows the scatterplot for the RED band, Fig. 8 displays the statistical graphs for the four indicators, and Table III shows the detailed indicator values

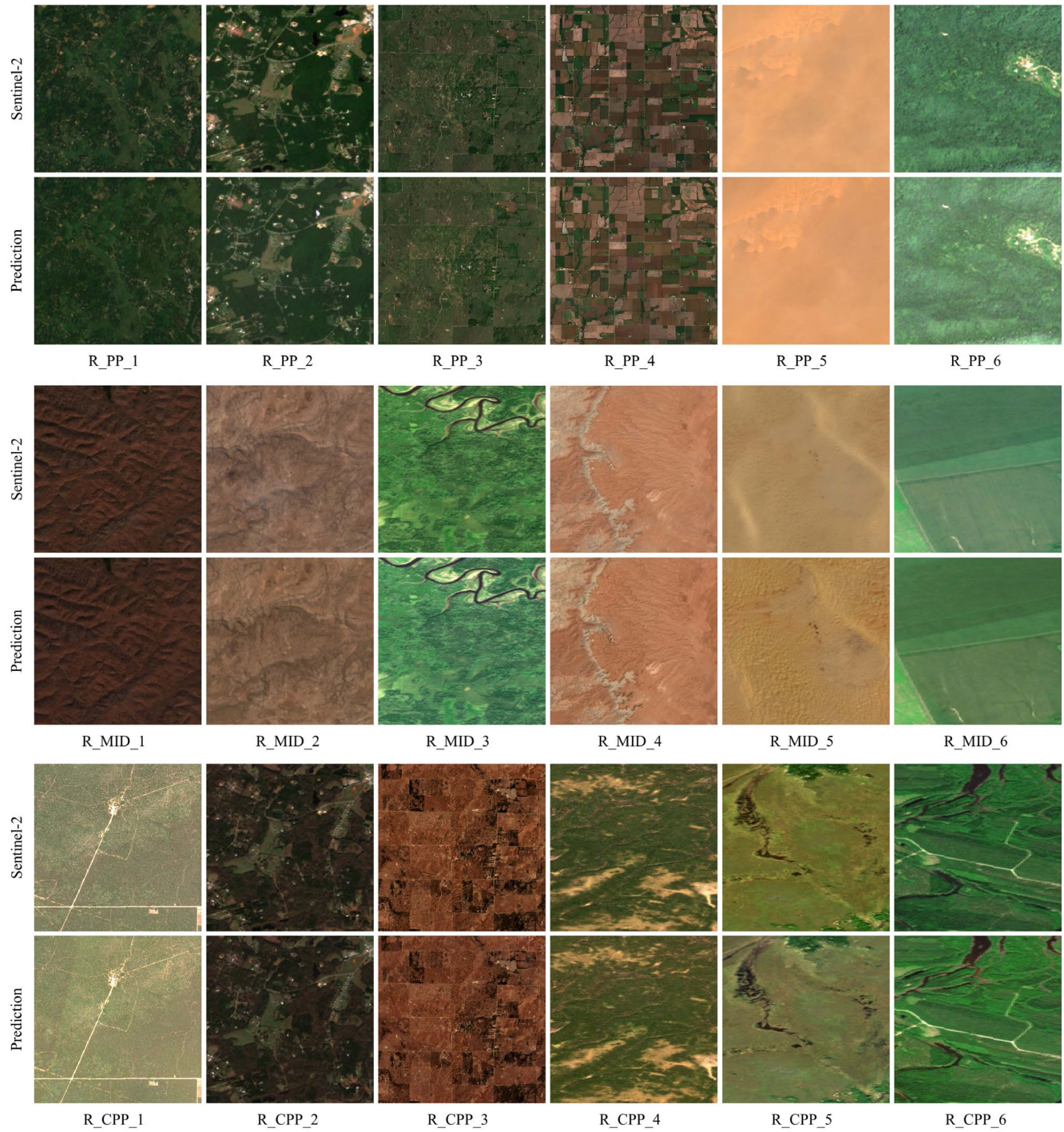

Fig. 5. Sentinel image at A2 and downscale prediction scatter plots (RED band, true-color compositing). The stretching range of the same region and three bands remains unchanged. True-color composition: 0–0.1: R_PP_6, R_MID_3, RR_MID_6, R_CPP_1, R_CPP_4, R_CPP_5, R_CPP_6; 0–0.5: R_PP_5, R_MID_4, R_MID_5; 0–0.3: others.

(corresponding values for the NIR bands are shown in Figs. 9 and 10, and Table IV).

In terms of the quantitative assessment, the RMSE was less than 0.04 for both bands across a total of 36 image pairs, while the majority (>85%) of the values were less than 0.02, with small fluctuations. The RED band demonstrated a maximum value of 0.0295 (R_MID_4) and a minimum value of 0.0028 (R_CPP_5). For the NIR bands, the values were 0.0355 (N_MID_3) and 0.0067 (N_CPP_6).

The nRMSE, which normalizes the average reflectance intensity of the image, was under 40% in both bands, with the majority (>85%) being below 20%. The nRMSE in the RED band ranged from 2.29% (R_PP_5) to 38.50% (R_PP_6), whereas that in the NIR band ranged from 2.23% (N_PP_4) to 10.96% (N_CPP_2).

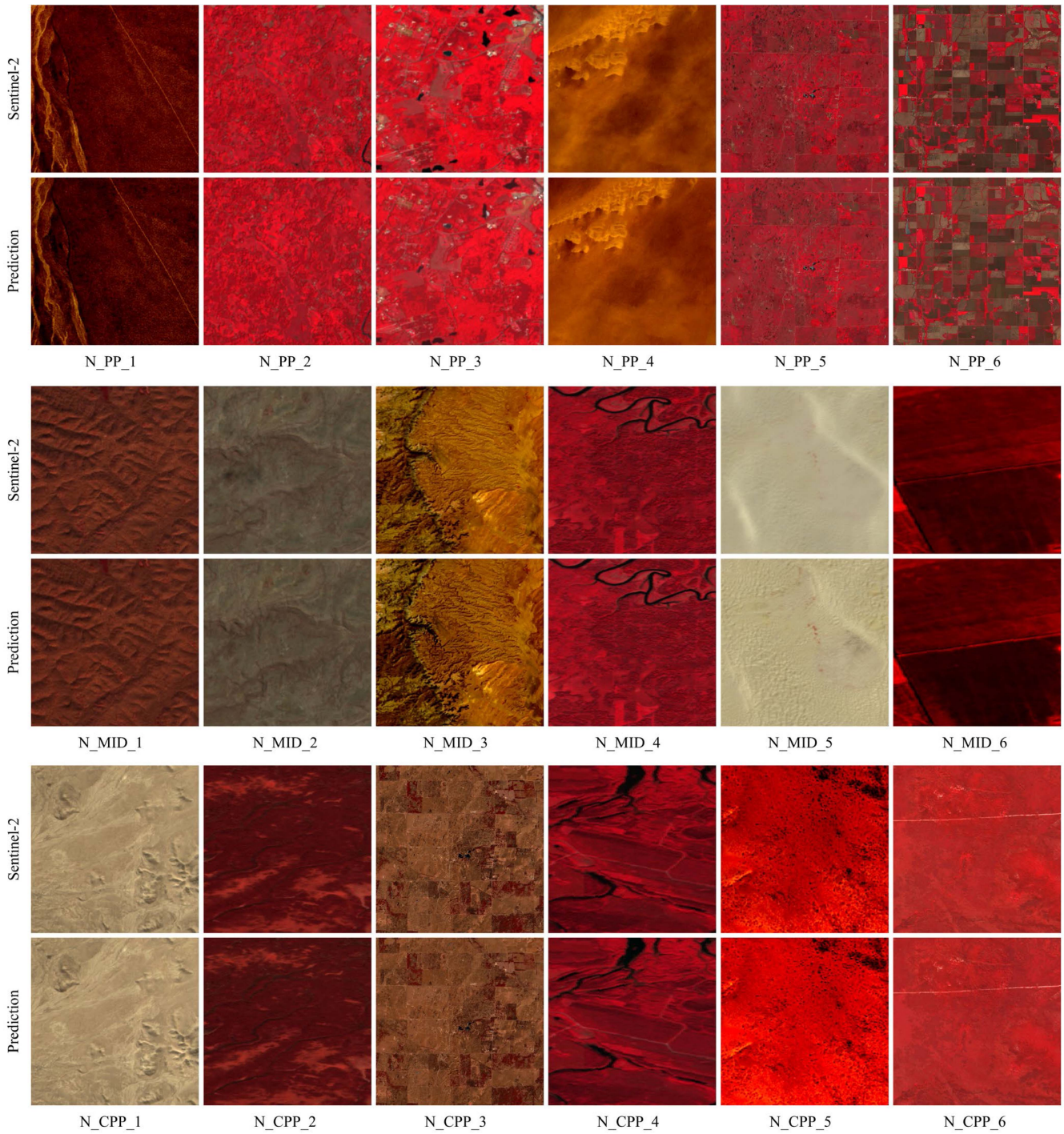

Fig. 6. Sentinel image A2 truth and downscale prediction images (NIR band, false-color compositing). The stretching range of the same region and three bands remains unchanged. False-color composition: 0–0.2: N_CPP_6; 0.3–0.5: N_PP_1, N_MID_3; 0.4–0.6: N_PP_4; 0.2–0.5: N_MID_6; 0.2–0.3: N_CPP_5; 0–0.5: others.

The nRMSE in the NIR band was significantly lower due to the higher average reflectance in the NIR band than in the RED band.

The bias was less than 0.02 in both bands, with smaller variation ranging from 0.0005 (R_CPP_5) to 0.0119 (R_PP_4) and 0.0003 (N_CPP_3) to 0.0175 (N_PP_6), indicating that FSDAF can effectively and precisely perform estimations under a wide variety of solar-viewing angles and AFXs. The bias in the NIR band was slightly higher than that in the RED band.

R^2 was greater than 0.7 throughout the majority (>85%) of the two bands, exhibiting a slightly greater variability compared to the other metrics. This value indicates the degree of confidence in the linear correlation between the predicted and true values, reflecting the aggregation trend and shape of the

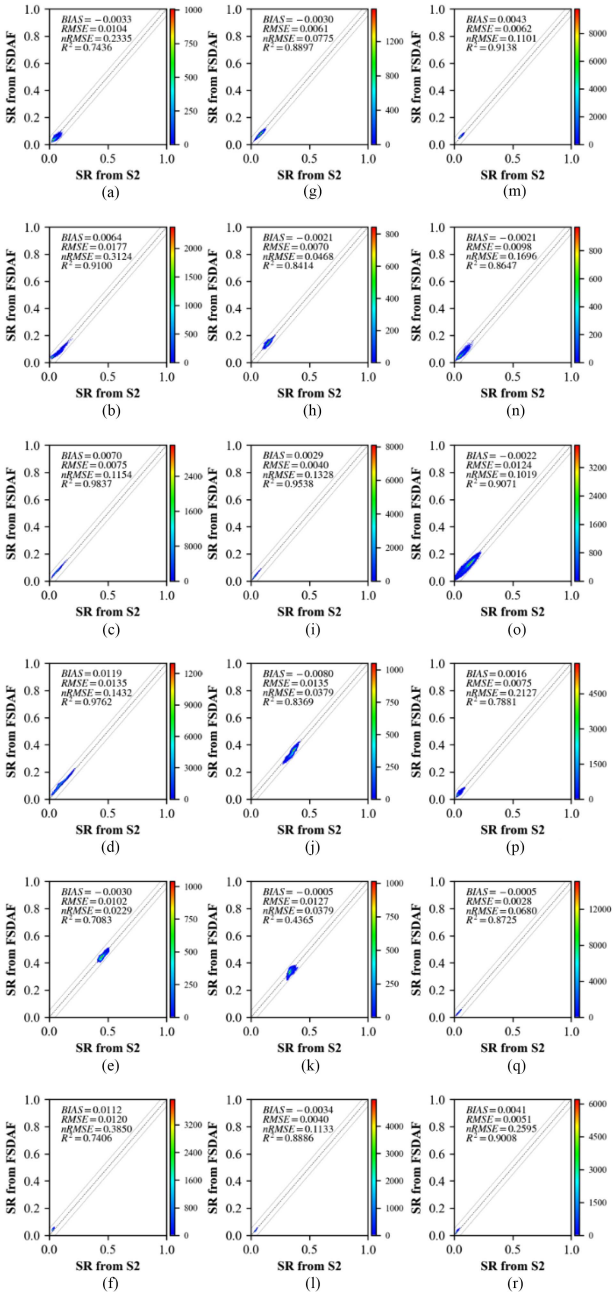

Fig. 7. Scatter plots of sentinel image at A2 and downscale prediction images (RED band). (a) R_PP_1. (b) R_PP_2. (c) R_PP_3. (d) R_PP_4. (e) R_PP_5. (f) R_PP_6. (g) R_MID_1. (h) R_MID_2. (i) R_MID_3. (j) R_MID_4. (k) R_MID_5. (l) R_MID_6. (m) R_CPP_1. (n) R_CPP_2. (o) R_CPP_3. (p) R_CPP_4. (q) R_CPP_5. (r) R_CPP_6.

scatterplot. The highest value in the RED band was 0.9837 (R_PP_3), while the lowest was 0.4365 (R_MID_5). The highest value in the NIR bands was 0.9953 (N_PP_6), while the lowest was 0.4645 (N_MID_5). Both R_MID_5 and N_MID_5 were situated within the same desert region with relatively higher reflectance and a smaller data range than other regions, and the surface texture varied between the two Sentinel images, resulting in a significantly lower R^2 compared to that of the others.

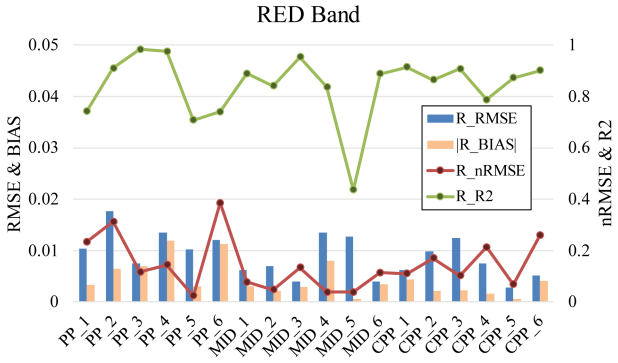

Fig. 8. Accuracy indicators of downscale prediction images (RED band). RMSE and BIA use the left *Y*-axis, nRMSE and R2 correspond to the right *Y*-axis.

TABLE III
ACCURACY INDICATORS OF DOWNSCALE PREDICTION IMAGES (RED BAND)

	RMSE	nRMSE	R2	BIAS	|BIAS|
R_PP_1	0.0104	0.2335	0.7436	−0.0033	0.0033
R_PP_2	0.0177	0.3124	0.91	0.0064	0.0064
R_PP_3	0.0075	0.1154	0.9837	0.007	0.007
R_PP_4	0.0135	0.1432	0.9762	0.0119	0.0119
R_PP_5	0.0102	0.0229	0.7083	−0.003	0.003
R_PP_6	0.012	0.385	0.7406	0.0112	0.0112
R_MID_1	0.0061	0.0775	0.8897	−0.003	0.003
R_MID_2	0.007	0.0468	0.8414	−0.0021	0.0021
R_MID_3	0.004	0.1328	0.9538	0.0029	0.0029
R_MID_4	0.0135	0.0379	0.8369	−0.008	0.008
R_MID_5	0.0127	0.0379	0.4365	−0.0005	0.0005
R_MID_6	0.004	0.1133	0.8886	−0.0034	0.0034
R_CPP_1	0.0062	0.1101	0.9138	0.0043	0.0043
R_CPP_2	0.0098	0.1696	0.8647	−0.0021	0.0021
R_CPP_3	0.0124	0.1019	0.9071	−0.0022	0.0022
R_CPP_4	0.0075	0.2127	0.7881	0.0016	0.0016
R_CPP_5	0.0028	0.068	0.8725	−0.0005	0.0005
R_CPP_6	0.0051	0.2595	0.9008	0.0041	0.0041

C. Sensitivity to the Distribution of Angles and AFX

The mean values of each parameter for both bands in the PP, MID, and CPP groups are shown in Fig. 11 and Table V.

Notably, the nRMSE and R^2 values were consistently stable across all groups. This suggests that the fusion method holds potential for application across a wide range of anisotropic scenarios while maintaining stable prediction accuracy.

Regarding the comparison between the PP/CPP/MID groups and their solar-viewing angle transition from the PP to MID, and then to the CPP group, the RMSE reached 0.0119, 0.0079, and 0.0073. The corresponding biases were 0.0071, 0.0033, and 0.0025 in the RED band. In the NIR band, the RMSE values were 0.0195, 0.0140, and 0.0133 with biases of 0.0095, 0.0076, and 0.0054. Both bands exhibited a consistent trend.

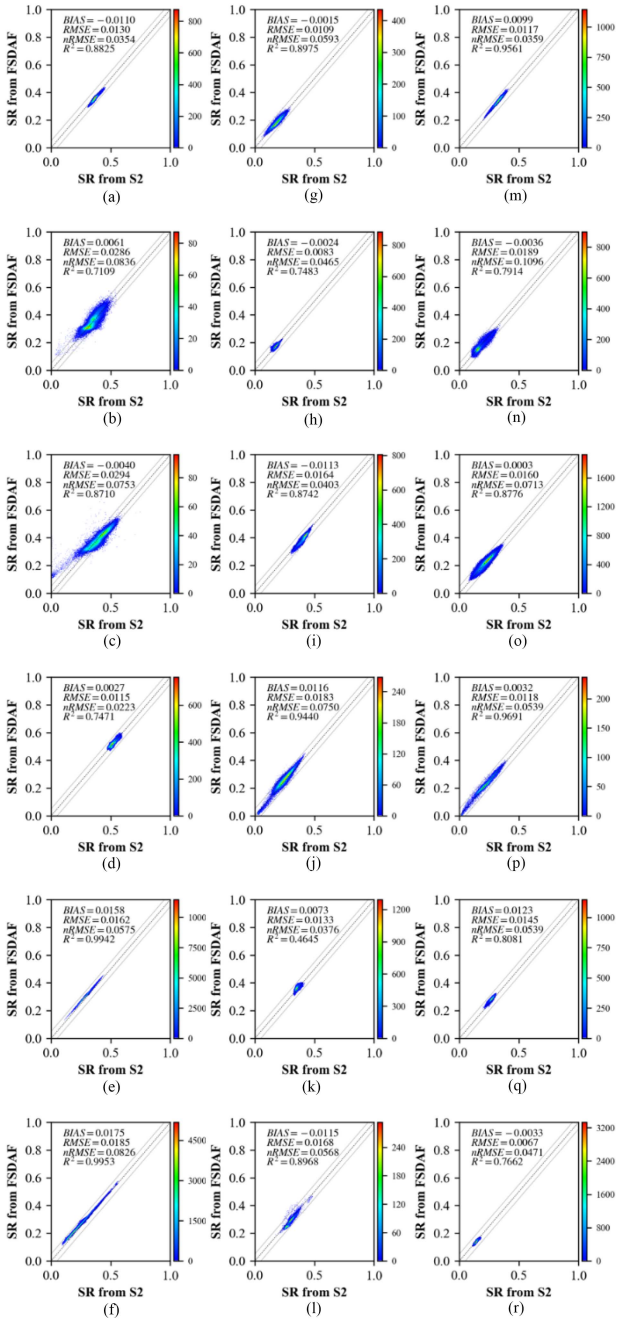

Fig. 9. Scatter plots of sentinel image at A2 and downscale prediction images (NIR band). (a) N_PP_1. (b) N_PP_2. (c) N_PP_3. (d) N_PP_4. (e) N_PP_5. (f) N_PP_6. (g) N_MID_1. (h) N_MID_2. (i) N_MID_3. (j) N_MID_4. (k) N_MID_5. (l) N_MID_6. (m) N_CPP_1. (n) N_CPP_2. (o) N_CPP_3. (p) N_CPP_4. (q) N_CPP_5. (r) N_CPP_6.

The PP group exhibited the most drastic changes in BRDF; thus, high-resolution reflectance changes were more difficult to characterize using low-resolution BRDF, resulting in more biased predictions. In contrast, as the solar-viewing angle transitioned to the MID and CPP planes, where BRDF shape variations were comparatively smaller, the reflectance changes due to identical VZA changes were less pronounced, and the prediction accuracy improved.

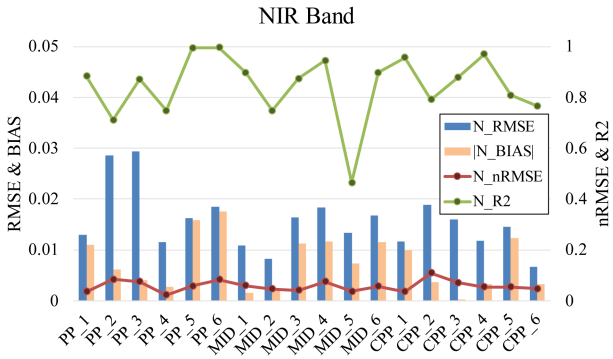

Fig. 10. Accuracy indicators of downscale prediction images (NIR band). RMSE and bias use the left *Y*-axis, nRMSE and R2 correspond to the right Y-axis.

TABLE IV
ACCURACY INDICATORS OF DOWNSCALE PREDICTION IMAGES (NIR BAND)

	RMSE	nRMSE	R2	BIAS	|BIAS|
N_PP_1	0.013	0.0354	0.8825	−0.011	0.011
N_PP_2	0.0286	0.0836	0.7109	0.0061	0.0061
N_PP_3	0.0294	0.0753	0.871	−0.004	0.004
N_PP_4	0.0115	0.0223	0.7471	0.0027	0.0027
N_PP_5	0.0162	0.0575	0.9942	0.0158	0.0158
N_PP_6	0.0185	0.0826	0.9953	0.0175	0.0175
N_MID_1	0.0109	0.0593	0.8975	−0.0015	0.0015
N_MID_2	0.0083	0.0465	0.7483	−0.0024	0.0024
N_MID_3	0.0164	0.0403	0.8742	−0.0113	0.0113
N_MID_4	0.0183	0.075	0.944	0.0116	0.0116
N_MID_5	0.0133	0.0376	0.4645	0.0073	0.0073
N_MID_6	0.0168	0.0568	0.8968	−0.0115	0.0115
N_CPP_1	0.0117	0.0359	0.9561	0.0099	0.0099
N_CPP_2	0.0189	0.1096	0.7914	−0.0036	0.0036
N_CPP_3	0.016	0.0713	0.8776	0.0003	0.0003
N_CPP_4	0.0118	0.0539	0.9691	0.0032	0.0032
N_CPP_5	0.0145	0.0539	0.8081	0.0123	0.0123
N_CPP_6	0.0067	0.0471	0.7662	−0.0033	0.0033

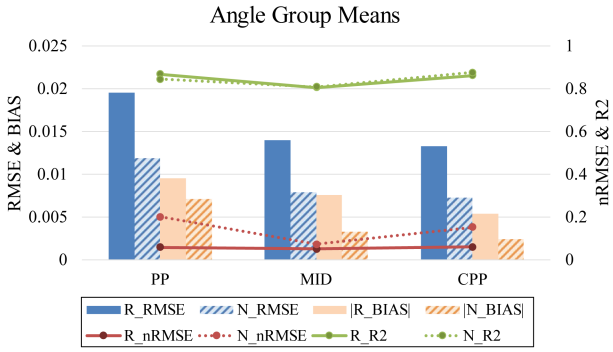

Fig. 11. Mean accuracy indicators of solar-viewing angle groups. RMSE and bias use the left *Y*-axis, nRMSE and R2 correspond to the right *Y*-axis.

TABLE V
MEAN ACCURACY INDICATORS OF DOWNSCALE PREDICTION IMAGES FOR ANGLE GROUP

	RMSE	nRMSE	R2	BIAS	|BIAS|
RED BAND					
PP_MEAN	0.0119	0.2021	0.8437	0.0050	0.0071
MID_MEAN	0.0079	0.0744	0.8078	–0.0024	0.0033
CPP_MEAN	0.0073	0.1536	0.8745	0.0009	0.0025
NIR BAND					
PP_MEAN	0.0195	0.0595	0.8668	0.0045	0.0095
MID_MEAN	0.0140	0.0526	0.8042	–0.0013	0.0076
CPP_MEAN	0.0133	0.0620	0.8614	0.0031	0.0054

The PP/MID/CPP mean is the mean value of each solar-viewing angle group.

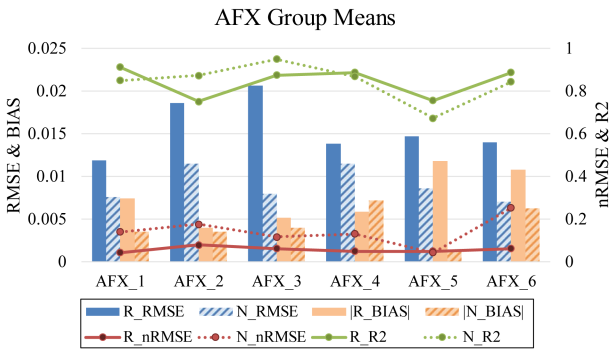

Fig. 12. Mean accuracy indicators of AFX groups. RMSE and bias use the left *Y*-axis, nRMSE and R2 correspond to the right *Y*-axis.

The mean metrics for the six AFX groups are presented in Fig. 12 and Table VI.

In the comparison among the different AFX prototype classification groups, the RMSE tended to increase and then decrease as the AFX increased. Concerning the RMSE, there appears to be an assumption that for smaller AFX values (when geometric-optical scattering is dominant and the shape of BRDF is roof-like), the MODIS reflectance changes become more pronounced. This effect brings the MODIS reflectance changes closer to those observed in Sentinel data; the larger the AFX (when volumetric scattering is dominant and the BRDF is bowl-like in shape), the reflectance changes for both resolutions tend to flatten out, and the discrepancy between the predicted results and the true value also decreases. In contrast, the intermediate interaction types are likely not similarly proportioned at the two scales, resulting in a lower accuracy for the intermediate category, where the scale effects are most pronounced.

The bias metric exhibited different trends in contrast to the RMSE. When comparing the RED and NIR bands, the bias trends were also inconsistent. Bias decreased and then increased in the RED band, whereas it was relatively more stable in the NIR band (with notably low values at AFX_5).

These also provide new evidence for the weak coupling between AFX, IGBP and NDVI. R_PP_3 and R_CPP_3 represent the same region but in different seasons. Under the influence of phenological effects, their NDVI changes remarkably, yet they still belong to the same AFX group. N_PP_5 and N_CPP_3 correspond to the same region in different seasons. However, their AFX group changed. In addition, the AFX of the same IGBP type are not always the same; R_PP_6 and R_MID_1 belong to the same deciduous broadleaf forest, but it is obvious from the visual inspection that their vegetation status is very different, which leads to a drastic change in their AFX classification. The Woody Savannas type, on the other hand, is assigned to more AFX categories and contains all conditions excluding AFX-5. Whereas the barren and dense vegetation are more concentrated in the extremes of AFX-5 or AFX-6, however, their NDVI levels vary greatly.

TABLE VI
MEAN ACCURACY INDICATORS OF DOWNSCALE PREDICTION IMAGES FOR AFX GROUP

	RMSE	nRMSE	R2	BIAS	|BIAS|
RED BAND					
AFX_1_MEAN	0.0076	0.1404	0.8490	–0.0007	0.0035
AFX_2_MEAN	0.0115	0.1763	0.8720	0.0007	0.0035
AFX_3_MEAN	0.0080	0.1167	0.9482	0.0026	0.0040
AFX_4_MEAN	0.0115	0.1313	0.8671	0.0018	0.0072
AFX_5_MEAN	0.0086	0.0429	0.6724	–0.0013	0.0013
AFX_6_MEAN	0.0070	0.2526	0.8433	0.0040	0.0062
NIR BAND					
AFX_1_MEAN	0.0119	0.0435	0.9120	–0.0009	0.0075
AFX_2_MEAN	0.0186	0.0799	0.7502	0.0001	0.0040
AFX_3_MEAN	0.0206	0.0623	0.8743	–0.0050	0.0052
AFX_4_MEAN	0.0139	0.0504	0.8867	0.0058	0.0058
AFX_5_MEAN	0.0147	0.0497	0.7556	0.0118	0.0118
AFX_6_MEAN	0.0140	0.0622	0.8861	0.0009	0.0108

The AFX mean calculates the mean of each AFX group.

V. DISCUSSION

In addition to the aforementioned factors, the errors in this method may originate from atmospheric corrections, resampling operations, assumptions of surface stability, and errors in FSDAF processing. The evaluation of fusion accuracy across various test areas further substantiates the presence of scale differences and topographic effects of the BRDF.

A. *Scale Difference of BRDF*

A previous article analyzed the scale effects of BRDF within the range of 6–7 km and 500 m, using POLDER and MODIS BRDF data [51]. The higher resolution MODIS exhibited the same six BRDF archetypes as POLDER, capturing some of the more extreme BRDF shapes. The results of this article demonstrate that this phenomenon persists between MODIS and higher resolution Sentinel data.

Although the highest available resolution of the BRDF (MCD43A1) data was used, compared to the more common Landsat MODIS fusion task (which exhibits a scale difference of 480:30 = 16), the considerably 48-fold scale difference still

poses a fusion challenge. Although the fusion strategy proposed in this article achieved consistent accuracy over a wide AFX range, it could only partially simulate the variation trend of the BRDF. The large-scale difference between MODIS and Sentinel, affecting the representativeness of the BRDF within the target heterogeneous pixels, may indicate that uncertainties arise when directly applying the 480-m BRDF to the 10/30 m scale. As a result, despite the robust fusion accuracy (low bias), the fusion is unable to adequately capture reflectance trends at high resolutions (relatively higher RMSE), which also implies that the drastic BRDF changes at the 10-m scale surpass those of the reference (480 m).

All experiments in this article were performed within a narrow variation in VZA of the Sentinel (10.3°), similar to the conclusions drawn from Landsat (7.5°) [52]; however, the reflectance variability resulting from the combined effect of the solar-viewing angle and BRDF is not negligible.

To enhance the accuracy of remote sensing inversion applications and correct satellite image BRDF, an a priori knowledge database for higher resolution is necessary. Referring to the MODIS BRDF data development process, the BRDF inversion with insufficient angular samples is based on accumulated background BRDF information and an archetype database [53]. A further step toward enhancing and evaluating this angular reflectance downscaling may involve obtaining a preliminary estimation at a finer resolution and utilizing it in the fusion processing again for error iteration and control to optimize the results.

B. Topography Effect in Terrains

We discovered that the terrain (R_MID_4 or N_MID_3, which are in the same region) and dune desert regions (R_MID_5 or N_MID_5) had larger prediction errors, primarily due to the influence of topography.

In general, topographic effects can significantly influence the shape and intensity of the surface BRDF by changing the local solar-viewing geometry at the subpixel level. When the solar-viewing angle of the entire pixel was fixed, the determining factor for the BRDF change was the mean slope. As the mean slope increased, the changes in the BRDF due to topography gradually increased [54]. The mean slopes of the same surface at different resolutions were almost identical, and coarser resolutions attenuated the mean slope, whereas the mean slope increased at finer resolutions. Thus, terrains at 500 m had little impact on the BRDF shape and became subpixel information. However, the slope at 10 m could drastically change the angular relationship. In this fusion method, given that the BRDF shapes of the two scales were identical and homogeneous, the difference in the local solar-viewing angle caused a discrepancy in the reflectance.

To further optimize the results, the inclusion of a digital elevation model for local solar-viewing angle calculation, or the use of the BRDF model designed for topographical conditions, can be considered as two potential optimization methods. Over the past decade, there has been a noticeable trend in research focusing on topographical correction and BRDF modeling.

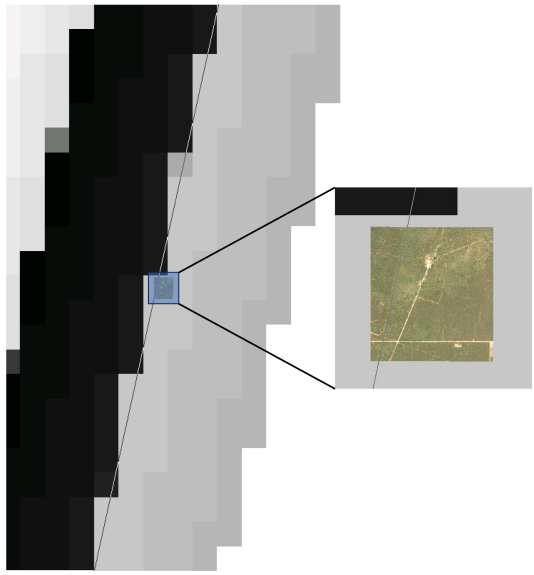

Fig. 13. Unsampled VAA of the Sentinel-2 scene and image of R_CPP_1 region.

Compared to the RTLSR model, kernel-driven BRDF models for terrain (i.e., Topo-KD) are more suitable for modeling the BRDF under varying topography, particularly for finer pixels with more pronounced terrain variations [55].

C. Abnormality

In reference to the abnormal stripe observed in the prediction of R_CPP_1, we examined the input of the Sentinel-2 image at Angle-1 and found that this stripe also appeared in the input data, indicating that this phenomenon was related to the sensing process of the Sentinel-2 satellites.

Based on the aforementioned description of the Sentinel data acquired using multiple detectors, Fig. 13 shows the specific location and details of the unsampled raw VAA grid (5-km resolution) for Sentinel-2, as well as the experimental region corresponding to R_CPP_1, demonstrating that the stripe at A1 does indeed coincide with the region where the two detectors meet. The difference in the VAA between the two regions was approximately 14.8°, and it appears that the reflectance variation under CPP conditions cannot be fully explained by this degree of VAA variation. This also serves as a reminder that the angle-induced variability in Sentinel data should be handled more cautiously when the pattern of change is unclear.

D. Limitations and Further Directions

During the study, we mainly encountered the problem that suitable large FOV satellite data for validation are limited. Served as an alternative in future, some other data sources and their attributes are listed as follows.

The primary source is data of satellites. The data from SPOT4 (take 5) [56], which is the precursor to the Sentinel-2 satellite, is the closest to the standards of Sentinel-2 and capable of reaching a maximum VZA of 25°; however, its data are no longer valid

and available. There are also EnMAP hyperspectral satellites available from 2022 [57], whose VZA can reach a maximum of 30° when pointing at a target and resolution is 30 m, but its swath is relatively small. The GaoFen-1 and GaoFen-6 WFV sensors, whose VZA can reach 35° and a resolution of 16 m, with two days revisit period, can be used as a suitable source of multiangle data in the areas where they frequently overpass [58].

In addition to satellite data, UAVs are one of the means of obtaining multiangle data. It is flexible and capable of acquiring angular reflectance in a small area with proper pattern control. Some studies using UAV data as a data source for BRDF research have already emerged [59]. We are actively preparing related experiments and expect to collect more range-flexible angular reflectance data. In spite of this, the difference in resolution between UAV and Sentinel-2 is drastic, and the difference between two sensors and atmospheric circumstances also make joint UAV and satellite validation difficult.

With the development of computer simulation technology and remote sensing radiative transfer modeling, research on the use of simulation data, which served as quantitative remote sensing validation data, has gradually increased. The most representative simulation software in remote sensing are DART [60] and LESS [61]. However, whether the results of simulated data can reflect the process of real satellite observation of the Earth needs further consideration.

Apart from data, this article's analysis and application of angular information are relatively rudimentary and may not represent the most optimal approach. There is still room for improvement in current spatiotemporal fusion algorithms within the present scenario. In improving the methodology of this article, there may be more efficient ways than utilizing BRDF-generated BRFs as direct inputs.

In introduction, a number of studies utilizing BRDFs for cross-scale applications were mentioned, where they performed an unmixing on the BRDF data itself that relied on pure pixels (or furthermore, the generation of a landcover-based LUT) for the purpose of downscaling. In fact, pure pixels of a single type of BRDF are not always available, and the generation of LUTs relies on the prior processing of a large amount of data. High-quality classification results are also necessary when applied at high resolution. It is important to note that these programs serve the generation of albedo products, which are derived from the integration of the BRDF over the hemisphere, and they may not be concerned with the accuracy of the reflectance in a specific direction.

Angle effect corrections for NBAR have also been published in studies that combine simplified BRDF shapes with C-factor methods. Some are averaged over all BRDFs, while others have performed prototype BRDF extraction according to AFX, so far these articles have achieved fair accuracy results for NBAR generation over a small VZA range. This may indicate that there is data redundancy in the existing way of utilizing MODIS BRDF data, and that appropriate simplification may have an acceptable impact on accuracy. Whether the simplified BRDF with C-factor method is still applicable to BRF generation under other angles needs further investigation.

In the research for downscaling algorithms, neural-network-based super-resolution reconstruction might also be an improvement strategy. The neural-network-based method learns the mapping relationship between low spatial resolution and high spatial resolution through the network structure to achieve the purpose of downscaling, and the existing researches contain SRCNN [62], FSRCNN [63], VDSR [64], EDSR [65], and SRGAN [66]. The main goal of existing neural network methods is natural picture generation, and there are fewer studies on remote sensing image reconstruction, and their magnification is difficult to reach the scale difference ($48\times$) in this article. Considering the data limitations mentioned earlier, the acquisition of samples also becomes problematic; applying them to angular reflectance downscaling requires careful consideration of the way angular information is introduced and the network design.

VI. Conclusion

The fusion-model-based method proposed in this article serves as an exploratory approach for downscaling low-resolution angular information into high-resolution satellite data and yielding high-resolution angular reflectance prediction results. Through validation using Sentinel-2 reflectance and MODIS BRDF data, the prediction accuracy of this method was found to be stable under a wide range of solar-viewing angles and AFX conditions.

In the sensitivity analysis of solar-viewing angles and AFX, the accuracy was predominantly influenced by variations in the solar-viewing angle, whereas the effects of surface AFX intensities were limited. When the solar-viewing angles transitioned from PP to MID and then to CPP, the RMSE values reached up to 0.0119, 0.0079, and 0.0073, accompanied by biases of 0.0071, 0.0033, and 0.0025 in the RED band (for the NIR band, the RMSE values were 0.0195, 0.0140, and 0.0133; the bias values were 0.0095, 0.0076, and 0.0054). However, the accuracy did not differ between different AFX conditions, which means that no significant relationship between the AFX and accuracy could be drawn from the results.

Our results also demonstrated relevant evidence regarding the scale effects of BRDF and topographic influences at two resolutions using Sentinel-2 and MODIS satellite data. The spatially smoothed BRDF at the MODIS scale could lead to errors in Sentinel-2 reflectance within heterogeneous MODIS pixels; under these circumstances, using a BRDF with higher resolution is necessary. Given that the mean slope generally increases from coarser to finer pixels, the local sun-viewing geometry changes drastically due to topographical effects. This, in turn, causes a discrepancy between the predicted and reference images. BRDF scale differences, sampling errors, topographical effects, atmospheric conditions, and processing procedures also affected the final results.

The main scope of this article is currently focused on the vegetation and land surface, and the method can be extended to high-resolution BRDF inversion data sources and other remote sensing inversions that have specific angular data requirements. We also intend to conduct multiangular experiments using UAVs or the GaoFen-6 satellite to obtain the reflectance at a finer

resolution, with which the fusion result at a larger VZA could be evaluated. In addition to this, the design of fusion algorithms that are more suitable for angular downscaling is also one of the goals of the future article.

REFERENCES

[1] F. E. Nicodemus, "Directional reflectance and emissivity of an opaque surface," *Appl. Opt.*, vol. 4, no. 7, pp. 767–775, 1965, doi: 10.1364/AO.4.000767.

[2] S. Wei, H. Fang, C. B. Schaaf, L. He, and J. M. Chen, "Global 500 m clumping index product derived from MODIS BRDF data (2001–2017)," *Remote Sens. Environ.*, vol. 232, Oct. 2019, Art. no. 111296, doi: 10.1016/j.rse.2019.111296.

[3] X. Yang, Y. Liu, Z. Wu, Y. Yu, F. Li, and W. Fan, "Forest age mapping based on multiple-resource remote sensing data," *Environ. Monit. Assessment*, vol. 192, no. 11, Oct. 2020, Art. no. 734, doi: 10.1007/s10661-020-08694-4.

[4] M. Chopping, Z. Wang, C. Schaaf, M. A. Bull, and R. R. Duchesne, "Forest aboveground biomass in the southwestern United States from a MISR multi-angle index, 2000–2015," *Remote Sens. Environ.*, vol. 275, Jun. 2022, Art. no. 112964, doi: 10.1016/j.rse.2022.112964.

[5] M. Chopping et al., "Large area mapping of southwestern forest crown cover, canopy height, and biomass using the NASA multiangle imaging spectro-radiometer," *Remote Sens. Environ.*, vol. 112, no. 5, pp. 2051–2063, May 2008, doi: 10.1016/j.rse.2007.07.024.

[6] Y. Wang et al., "A combined GLAS and MODIS estimation of the global distribution of mean forest canopy height," *Remote Sens. Environ.*, vol. 174, pp. 24–43, Mar. 2016, doi: 10.1016/j.rse.2015.12.005.

[7] A. Bertoncini, C. Aubry-Wake, and J. W. Pomeroy, "Large-area high spatial resolution albedo retrievals from remote sensing for use in assessing the impact of wildfire soot deposition on high mountain snow and ice melt," *Remote Sens. Environ.*, vol. 278, 2022, Art. no. 113101, doi: 10.1016/j.rse.2022.113101.

[8] X. Lin et al., "Estimating 10-m land surface albedo from Sentinel-2 satellite observations using a direct estimation approach with Google Earth Engine," *ISPRS J. Photogrammetry Remote Sens.*, vol. 194, pp. 1–20, 2022, doi: 10.1016/j.isprsjprs.2022.09.016.

[9] N. Longbotham, C. Chaapel, L. Bleiler, C. Padwick, W. J. Emery, and F. Pacifici, "Very high resolution multiangle urban classification analysis," *IEEE Trans. Geosci. Remote Sens.*, vol. 50, no. 4, pp. 1155–1170, Apr. 2012, doi: 10.1109/TGRS.2011.2165548.

[10] W. Lucht and P. Lewis, "Theoretical noise sensitivity of BRDF and albedo retrieval from the EOS-MODIS and MISR sensors with respect to angular sampling," *Int. J. Remote Sens.*, vol. 21, no. 1, pp. 81–98, 2000, doi: 10.1080/014311600211000.

[11] L. Guanter, L. Alonso, and J. Moreno, "A method for the surface reflectance retrieval from PROBA/CHRIS data over land: Application to ESA SPARC campaigns," *IEEE Trans. Geosci. Remote Sens.*, vol. 43, no. 12, pp. 2908–2917, Dec. 2005, doi: 10.1109/TGRS.2005.857915.

[12] M. J. Barnsley, J. J. Settle, M. A. Cutter, D. R. Lobb, and F. Teston, "The PROBA/CHRIS mission: A low-cost smallsat for hyperspectral multiangle observations of the earth surface and atmosphere," *IEEE Trans. Geosci. Remote Sens.*, vol. 42, no. 7, pp. 1512–1520, Jul. 2004, doi: 10.1109/TGRS.2004.827260.

[13] W. Wanner et al., "Global retrieval of bidirectional reflectance and albedo over land from EOS MODIS and MISR data: Theory and algorithm," *J. Geophys. Res.: Atmos.*, vol. 102, no. D14, pp. 17143–17161, 1997, doi: 10.1029/96JD03295.

[14] F. Jacob, A. Olioso, M. Weiss, F. Baret, and O. Hautecoeur, "Mapping short-wave albedo of agricultural surfaces using airborne PolDER data," *Remote Sens. Environ.*, vol. 80, no. 1, pp. 36–46, 2002, doi: 10.1016/S0034-4257(01)00265-6.

[15] B. Duchemin, "NOAA/AVHRR bidirectional reflectance: Modeling and application for the monitoring of a temperate forest," *Remote Sens. Environ.*, vol. 67, no. 1, pp. 51–67, 1999, doi: 10.1016/S0034-4257(98)00080-7.

[16] C. B. Schaaf et al., "First operational BRDF, albedo nadir reflectance products from MODIS," *Remote Sens. Environ.*, vol. 83, no. 1–2, pp. 135–148, Nov. 2002, doi: 10.1016/s0034-4257(02)00091-3.

[17] Y. Liu et al., "Evaluation of the VIIRS BRDF, Albedo and NBAR products suite and an assessment of continuity with the long term MODIS record," *Remote Sens. Environ.*, vol. 201, pp. 256–274, 2017, doi: 10.1016/j.rse.2017.09.020.

[18] O. Samain, J.-L. Roujean, and B. Geiger, "Use of a Kalman filter for the retrieval of surface BRDF coefficients with a time-evolving model based on the ECOCLIMAP land cover classification," *Remote Sens. Environ.*, vol. 112, no. 4, pp. 1337–1346, 2008, doi: 10.1016/j.rse.2007.07.007.

[19] Z. Yang, N. Lu, J. Shi, P. Zhang, C. Dong, and J. Yang, "Overview of FY-3 payload and ground application system," *IEEE Trans. Geosci. Remote Sens.*, vol. 50, no. 12, pp. 4846–4853, Dec. 2012, doi: 10.1109/TGRS.2012.2197826.

[20] M. Drusch et al., "Sentinel-2: ESA's optical high-resolution mission for GMES operational services," *Remote Sens. Environ.*, vol. 120, pp. 25–36, 2012, doi: 10.1016/j.rse.2011.11.026.

[21] M. A. Wulder et al., "Current status of Landsat program, science, and applications," *Remote Sens. Environ.*, vol. 225, pp. 127–147, 2019, doi: 10.1016/j.rse.2019.02.015.

[22] B. Jiang, S. Liang, J. R. Townshend, and Z. M. Dodson, "Assessment of the radiometric performance of Chinese HJ-1 satellite CCD instruments," *IEEE J. Sel. Topics Appl. Earth Observ. Remote Sens.*, vol. 6, no. 2, pp. 840–850, Apr. 2013, doi: 10.1109/JSTARS.2012.2212236.

[23] W. Xu, J. Gong, and M. Wang, "Development, application, and prospects for Chinese land observation satellites," *Geo-Spatial Inf. Sci.*, vol. 17, no. 2, pp. 102–109, 2014, doi: 10.1080/10095020.2014.917454.

[24] M. Wu, J. Jin, J. Wang, and Q. Wang, "Hyperspectral indices developed from multi-angular bidirectional reflectance can trace the particle size of granite," *Acta Geophys.*, vol. 71, no. 1, pp. 193–208, 2023, doi: 10.1007/s11600-022-00900-w.

[25] M. Danner, K. Berger, M. Wocher, W. Mauser, and T. Hank, "Retrieval of biophysical crop variables from multi-angular canopy spectroscopy," *Remote Sens.*, vol. 9, no. 7, 2017, Art. no. 726, doi: 10.3390/rs9070726.

[26] Y. Shuai, J. G. Masek, F. Gao, and C. B. Schaaf, "An algorithm for the retrieval of 30-m snow-free albedo from Landsat surface reflectance and MODIS BRDF," *Remote Sens. Environ.*, vol. 115, no. 9, pp. 2204–2216, 2011, doi: 10.1016/j.rse.2011.04.019.

[27] Y. Shuai, J. G. Masek, F. Gao, C. B. Schaaf, and T. He, "An approach for the long-term 30-m land surface snow-free albedo retrieval from historic Landsat surface reflectance and MODIS-based a priori anisotropy knowledge," *Remote Sens. Environ.*, vol. 152, pp. 467–479, 2014, doi: 10.1016/j.rse.2014.07.009.

[28] F. Gao, T. He, J. G. Masek, Y. Shuai, C. B. Schaaf, and Z. Wang, "Angular effects and correction for medium resolution sensors to support crop monitoring," *IEEE J. Sel. Topics Appl. Earth Observ. Remote Sens.*, vol. 7, no. 11, pp. 4480–4489, Nov. 2014, doi: 10.1109/JSTARS.2014.2343592.

[29] T. He, S. Liang, D. Wang, X. Chen, D.-X. Song, and B. Jiang, "Land surface albedo estimation from Chinese HJ satellite data based on the direct estimation approach," *Remote Sens.*, vol. 7, no. 5, pp. 5495–5510, May 2015, doi: 10.3390/rs70505495.

[30] Z. Jiao, M. J. Hill, C. B. Schaaf, H. Zhang, Z. Wang, and X. Li, "An anisotropic flat index (AFX) to derive BRDF archetypes from MODIS," *Remote Sens. Environ.*, vol. 141, pp. 168–187, 2014, doi: 10.1016/j.rse.2013.10.017.

[31] H. Zhang et al., "Reflectance anisotropy from MODIS for albedo retrieval from a single directional Reflectance," *Remote Sens.*, vol. 14, no. 15, Aug. 2022, Art. no. 3627, doi: 10.3390/rs14153627.

[32] D. P. Roy et al., "A general method to normalize Landsat reflectance data to nadir BRDF adjusted reflectance," *Remote Sens. Environ.*, vol. 176, pp. 255–271, Apr. 2016, doi: 10.1016/j.rse.2016.01.023.

[33] D. P. Roy, J. Li, H. K. Zhang, L. Yan, H. Huang, and Z. Li, "Examination of Sentinel-2A multi-spectral instrument (MSI) reflectance anisotropy and the suitability of a general method to normalize MSI reflectance to nadir BRDF adjusted reflectance," *Remote Sens. Environ.*, vol. 199, pp. 25–38, 2017, doi: 10.1016/j.rse.2017.06.019.

[34] M. Claverie et al., "The harmonized Landsat and Sentinel-2 surface reflectance data set," *Remote Sens. Environ.*, vol. 219, pp. 145–161, 2018, doi: 10.1016/j.rse.2018.09.002.

[35] B. Franch, E. F. Vermote, and M. Claverie, "Intercomparison of Landsat albedo retrieval techniques and evaluation against in situ measurements across the US SURFRAD network," *Remote Sens. Environ.*, vol. 152, pp. 627–637, 2014, doi: 10.1016/j.rse.2014.07.019.

[36] B. Franch et al., "A method for Landsat and Sentinel 2 (HLS) BRDF normalization," *Remote Sens.*, vol. 11, no. 6, 2019, Art. no. 632, doi: 10.3390/rs11060632.

[37] X. Zhu, F. Cai, J. Tian, and T. K.-A. Williams, "Spatiotemporal fusion of multisource remote sensing data: Literature survey, taxonomy, principles, applications, and future directions," *Remote Sens.*, vol. 10, no. 4, 2018, Art. no. 527, doi: 10.3390/rs10040527.

[38] X. Zhu, J. Chen, F. Gao, X. Chen, and J. G. Masek, "An enhanced spatial and temporal adaptive reflectance fusion model for complex heterogeneous regions," *Remote Sens. Environ.*, vol. 114, no. 11, pp. 2610–2623, 2010, doi: 10.1016/j.rse.2010.05.032.
[39] I. V. Emelyanova, T. R. McVicar, T. G. Van Niel, L. T. Li, and A. I. J. M. van Dijk, "Assessing the accuracy of blending Landsat–MODIS surface reflectances in two landscapes with contrasting spatial and temporal dynamics: A framework for algorithm selection," *Remote Sens. Environ.*, vol. 133, pp. 193–209, 2013, doi: 10.1016/j.rse.2013.02.007.
[40] B. Zhukov, D. Oertel, F. Lanzl, and G. Reinhackel, "Unmixing-based multisensor multiresolution image fusion," *IEEE Trans. Geosci. Remote Sens.*, vol. 37, no. 3, pp. 1212–1226, May 1999, doi: 10.1109/36.763276.
[41] M. Wu, Z. Niu, C. Wang, C. Wu, and L. Wang, "Use of MODIS and Landsat time series data to generate high-resolution temporal synthetic Landsat data using a spatial and temporal reflectance fusion model," *J. Appl. Remote Sens.*, vol. 6, no. 1, 2012, Art. no. 063507, doi: 10.1117/1.JRS.6.063507.
[42] J. Xue, Y. Leung, and T. Fung, "A Bayesian data fusion approach to spatio-temporal fusion of remotely sensed images," *Remote Sens.*, vol. 9, no. 12, 2017, Art. no. 1310, doi: 10.3390/rs9121310.
[43] D. Jia, C. Song, C. Cheng, S. Shen, L. Ning, and C. Hui, "A novel deep learning-based spatiotemporal fusion method for combining satellite images with different resolutions using a two-stream convolutional neural network," *Remote Sens.*, vol. 12, no. 4, 2020, Art. no. 698, doi: 10.3390/rs12040698.
[44] X. Zhu, E. H. Helmer, F. Gao, D. Liu, J. Chen, and M. A. Lefsky, "A flexible spatiotemporal method for fusing satellite images with different resolutions," *Remote Sens. Environ.*, vol. 172, pp. 165–177, 2016, doi: 10.1016/j.rse.2015.11.016.
[45] D. Jia, C. Cheng, C. Song, S. Shen, L. Ning, and T. Zhang, "A hybrid deep learning-based spatiotemporal fusion method for combining satellite images with different resolutions," *Remote Sens.*, vol. 13, no. 4, 2021, Art. no. 645, doi: 10.3390/rs13040645.
[46] B. Zhang, L. Zhang, D. Xie, X. Yin, C. Liu, and G. Liu, "Application of synthetic NDVI time series blended from Landsat and MODIS data for grassland biomass estimation," *Remote Sens.*, vol. 8, no. 1, 2015, Art. no. 10, doi: 10.3390/rs8010010.
[47] K. Jia et al., "Land cover classification of Landsat data with phenological features extracted from time series MODIS NDVI data," *Remote Sens.*, vol. 6, no. 11, pp. 11518–11532, 2014, doi: 10.3390/rs61111518.
[48] B. Chen, B. Huang, and B. Xu, "Multi-source remotely sensed data fusion for improving land cover classification," *ISPRS J. Photogrammetry Remote Sens.*, vol. 124, pp. 27–39, 2017, doi: 10.1016/j.isprsjprs.2016.12.008.
[49] J. Zhou et al., "Sensitivity of six typical spatiotemporal fusion methods to different influential factors: A comparative study for a normalized difference vegetation index time series reconstruction," *Remote Sens. Environ.*, vol. 252, 2021, Art. no. 112130, doi: 10.1016/j.rse.2020.112130.
[50] P. Elson et al., "SciTools/cartopy: V0. 20.2 (v0. 20.2)," *Zenodo*, 2022, doi: 10.5281/zenodo.1182735.
[51] Z. Jiao et al., "The influence of spatial resolution on the angular variation patterns of optical reflectance as retrieved from MODIS and POLDER measurements," *Remote Sens. Environ.*, vol. 215, pp. 371–385, 2018, doi: 10.1016/j.rse.2018.06.025.
[52] J. R. Nagol et al., "Bidirectional effects in Landsat reflectance estimates: Is there a problem to solve?," *ISPRS J. Photogrammetry Remote Sens.*, vol. 103, pp. 129–135, 2015, doi: 10.1016/j.isprsjprs.2014.09.006.
[53] Y. Jin et al., "Consistency of MODIS surface bidirectional reflectance distribution function and albedo retrievals: 1. Algorithm performance," *J. Geophys. Res.: Atmos.*, vol. 108, no. D5, 2003, doi: 10.1029/2002JD002803.
[54] J. Wen et al., "Characterizing land surface anisotropic reflectance over rugged terrain: A review of concepts and recent developments," *Remote Sens.*, vol. 10, no. 3, 2018, Art. no. 370, doi: 10.3390/rs10030370.
[55] K. Yan et al., "Extending a linear kernel-driven BRDF model to realistically simulate reflectance anisotropy over rugged terrain," *IEEE Trans. Geosci. Remote Sens.*, vol. 60, 2022, pp. 1–16, doi: 10.1109/tgrs.2021.3064018.
[56] O. Hagolle et al., "SPOT-4 (Take 5): Simulation of Sentinel-2 time series on 45 large sites," *Remote Sens.*, vol. 7, no. 9, pp. 12242–12264, 2015, doi: 10.3390/rs70912242.
[57] L. Guanter et al., "The EnMAP spaceborne imaging spectroscopy mission for earth observation," *Remote Sens.*, vol. 7, no. 7, pp. 8830–8857, 2015, doi: 10.3390/rs70708830.
[58] A. Yang et al., "Radiometric cross-calibration of the wide field view camera onboard gaofen-6 in multispectral bands," *Remote Sens.*, vol. 12, no. 6, 2020, Art. no. 1037, doi: 10.3390/rs12061037.
[59] H. Cao et al., "The method of multi-angle remote sensing observation based on unmanned aerial vehicles and the validation of BRDF," *Remote Sens.*, vol. 15, no. 20, 2023, Art. no. 5000, doi: 10.3390/rs15205000.
[60] Y. Wang et al., "DART-Lux: An unbiased and rapid Monte Carlo radiative transfer method for simulating remote sensing images," *Remote Sens. Environ.*, vol. 274, 2022, Art. no. 112973, doi: 10.1016/j.rse.2022.112973.
[61] J. Qi et al., "LESS: LargE-scale remote sensing data and image simulation framework over heterogeneous 3D scenes," *Remote Sens. Environ.*, vol. 221, pp. 695–706, 2019, doi: 10.1016/j.rse.2018.11.036.
[62] C. Dong, C. C. Loy, K. He, and X. Tang, "Image super-resolution using deep convolutional networks," *IEEE Trans. Pattern Anal. Mach. Intell.*, vol. 38, no. 2, pp. 295–307, Feb. 2016, doi: 10.1109/TPAMI.2015.2439281.
[63] C. Dong, C. C. Loy, and X. Tang, "Accelerating the super-resolution convolutional neural network," in *Proc. Eur. Conf. Comput. Vis.*, 2016, pp. 391–407, doi: 10.1007/978-3-319-46475-6_25.
[64] J. Kim, J. K. Lee, and K. M. Lee, "Accurate image super-resolution using very deep convolutional networks," in *Proc. IEEE Conf. Comput. Vis. Pattern Recognit.*, 2016, pp. 1646–1654.
[65] B. Lim, S. Son, H. Kim, S. Nah, and K. M. Lee, "Enhanced deep residual networks for single image super-resolution," in *Proc. IEEE Conf. Comput. Vis. Pattern Recognit. Workshops*, 2017, pp. 1132–1140.
[66] C. Ledig et al., "Photo-realistic single image super-resolution using a generative adversarial network," in *Proc. IEEE Conf. Comput. Vis. Pattern Recognit.*, 2017, pp. 105–114.

Man Liang received the B.E. degree in remote sensing science and technology from the Wuhan University, Wuhan, China, in 2021. She is currently working toward the M.S. in cartography and geographic information system with the Aerospace Information Research Institute, Chinese Academy of Sciences, Beijing, China.

Her research interests include BRDF application, multiangular remote sensing, and inversion of quantitative remote sensing.

Xingfa Gu received the B.S. degree in surveying and mapping from the Wuhan University, Wuhan, China, in 1982, and the Ph.D. degree in remote sensing of physics from the University of Paris VII, Paris, France, in 1991.

He is currently a Professor with the Aerospace Information Research Institute, Chinese Academy of Sciences, Beijing, China. His research interests include radiometric calibration and atmospheric remote sensing.

Dr. Gu is an Academician of the International Academy of Astronautics.

Yan Liu received the B.S. degree in GIS and remote sensing from Lanzhou University, Lanzhou, China, in 2009, the M.S. degree in remote sensing from the Beijing Normal University, Beijing, China, in 2012, and the Ph.D. degree in environmental science from the University of Massachusetts, Boston, Boston, MA, USA, in 2016.

She is currently an Assistant Research Fellow with the Aerospace Information Research Institute, Chinese Academy of Sciences, Beijing, China. Her research interests include data fusion, BRDF inversion and application, and phenology monitoring using multiply scales data.

Tianhai Cheng received the B.S. degree in surveying and mapping engineering from Henan Polytechnic University, Jiaozuo, China, in 2004, and the Ph.D. degree in cartography and geographic information systems from the University of Chinese Academy of Sciences, Beijing, China, in 2009.

He is currently a Professor with the State Key Laboratory of Remote Sensing Science, Institute of Remote Sensing and Digital Earth, Chinese Academy of Sciences, Beijing, China. His research interests include atmospheric polarization remote sensing.

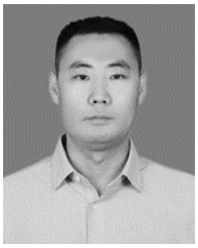

Hongtao Cao received the Ph.D. degree in cartography and geographic information systems from the Aerospace Information Research Institute, Chinese Academy of Sciences, Beijing, China, in June 2022.

He is currently a Research Assistant with the Academy of Ecological Civilization Development for JING-JIN-JI, Tianjin Normal University, Tianjin, China. His research interests include computational imaging, remote sensing radiometric calibration, and image processing.

Hu Zhang received the B.S. degree from the Shandong Jianzhu University, Jinan, China, in 2009, and the M.S. and Ph.D. degrees in geography from the Beijing Normal University, Beijing, China, in 2012 and 2015, respectively.

He is currently an Associate Professor with the School of Geographic and Environmental Sciences, Tianjin Normal University, Tianjin, China. His research interests include land surface reflectance anisotropy classification and land surface albedo retrieval based on prior knowledge.

Qian Zhang received the B.S. degree in remote sensing from the Wuhan University, Wuhan, China, in 2022. She is currently working toward the Ph.D. degree in geographic information system with the Aerospace Information Research Institute, University of Chinese Academy of Sciences, Beijing, China.

Her research interests include phenology and cloud detection.

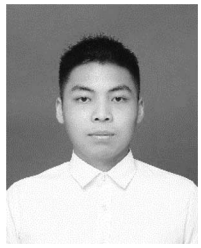

Yaozong Ding received the B.S. degree in surveying and mapping engineering from the HoHai University, Nanjing, China, in 2022. He is currently working toward the master's degree in geographic information system with the Aerospace Information Research Institute, University of Chinese Academy of Sciences, Beijing, China.

His research includes spatial and temporal fusion of remote sensing images and surface reflectance inversion.

Min Gao received the master's degree in natural resources and environment from the Aerospace Information Research Institute, Chinese Academy of Sciences, Beijing, China, in 2023.

Her research interests include spatiotemporal fusion method of remote sensing.

Xiangqin Wei received the Ph.D. degree in cartography and geography information system from the Institute of Remote Sensing and Digital Earth, Chinese Academy of Sciences, Beijing, China, in 2017.

She is currently an Associate Professor with the Aerospace Information Research Institute, Chinese Academy of Sciences, and the Remote Sensing Satellite Applications National Engineering Laboratory, Beijing, China. Her research interests include ecosystem remote sensing and application of quantitative remote sensing.

Yulin Zhan received the B.S. and M.S. degrees from the Nanchang University, Nanchang, China, in 1998 and 2002, respectively, and the Ph.D. degree in remote sensing & GIS from University of Chinese Academy of Sciences, Beijing, China, in 2005.

He is currently an Associate Researcher with the Aerospace Information Research Institute, Chinese Academy of Sciences, Beijing, China. His research interests include data fusion, crop classification, and remote sensing of the urban environment.